

16. M. R. House, *Nature* **313**, 17 (1985).  
 17. J. J. Sepkoski Jr., in *Global Events and Event Stratigraphy*, O. H. Walliser, Ed. (Springer-Verlag, Berlin, 1996), pp. 35–51.  
 18. J. A. Talent, R. Maulson, A. S. Andrew, J. Hamilton, D. J. Whitford, *Palaeogeogr. Palaeoclimatol. Palaeoecol.* **104**, 139 (1993).  
 19. K. J. Hsü *et al.*, *Nature* **316**, 809 (1985).  
 20. G. R. Dickens, J. R. O'Neill, D. K. Rea, R. M. Owen, *Paleoceanography* **10**, 965 (1995).  
 21. L. R. Kump, *Geology* **19**, 299 (1991).  
 22. K. A. Kvenvolden, *Rev. Geophys.* **31**, 173 (1993).  
 23. H. Irwin, C. Curtis, M. Coleman, *Nature* **269**, 209 (1977).  
 24. Funding was provided by grants from NSF and the American Chemical Society, and the Petroleum Research Fund to B.B.E. and R.E.C. We thank G. Byerly for his help with description of microspherules and microcryst grains and with the microprobe interpretations, we thank R. Ferrell for attempting

x-ray diffraction analysis of microspherules; we thank both for critical review of the manuscript.

**Supporting Online Material**  
[www.sciencemag.org/cgi/content/full/300/5626/1730/DC1](http://www.sciencemag.org/cgi/content/full/300/5626/1730/DC1)  
 Materials and Methods  
 Figs. S1 and S2  
 Table S1

16 December 2002; accepted 14 May 2003

# Holocene Forcing of the Indian Monsoon Recorded in a Stalagmite from Southern Oman

Dominik Fleitmann,<sup>1\*</sup> Stephen J. Burns,<sup>2</sup> Manfred Mudelsee,<sup>3</sup> Ulrich Neff,<sup>4</sup> Jan Kramers,<sup>1</sup> Augusto Mangini,<sup>4</sup> Albert Matter<sup>1</sup>

A high-resolution oxygen-isotope record from a thorium-uranium–dated stalagmite from southern Oman reflects variations in the amount of monsoon precipitation for the periods from 10.3 to 2.7 and 1.4 to 0.4 thousand years before the present (ky B.P.). Between 10.3 and 8 ky B.P., decadal to centennial variations in monsoon precipitation are in phase with temperature fluctuations recorded in Greenland ice cores, indicating that early Holocene monsoon intensity is largely controlled by glacial boundary conditions. After ~8 ky B.P., monsoon precipitation decreases gradually in response to changing Northern Hemisphere summer solar insolation, with decadal to multidecadal variations in monsoon precipitation being linked to solar activity.

Although lake [e.g. (1–3)] and marine [e.g. (4, 5)] records uniformly indicate that a major intensification in Indian Ocean monsoon (IOM) occurred at ~10 ky B.P., discrepancies exist about the timing and nature of changes in IOM intensity later in the Holocene. Because the IOM plays an important role in the global hydrological and energy cycles, a key question is whether the IOM weakened gradually or abruptly during the middle to late Holocene. Furthermore, because of low temporal resolution and age uncertainties of almost all continental paleomonsoon records, there is little consensus about the timing and causes of centennial- and decadal-scale fluctuations in monsoon precipitation. Previous studies on stalagmites from Oman have shown that oxygen-isotope profiles can provide more detailed information about the timing and causes of IOM variability (6, 7), but these records cover relatively short time intervals and not the entire Holocene. Here, we present a  $\delta^{18}\text{O}$  monsoon record from a stalagmite from Southern Oman, which continuously covers the time interval from 10.3 to 2.7 ky B.P. and 1.4 to 0.4 ky B.P. with an average time resolution of between 4 and

5 years. The temporal range and resolution allow a precise reconstruction of changes in IOM precipitation and intensity on subdecadal to millennial time scales.

Stalagmite Q5 was collected from Qunf Cave (17°10'N, 54°18'E; 650 m above sea level) in Southern Oman (fig. S1A). The area is suitable to study the IOM for two reasons. First, Qunf Cave sits at the present northern limit of the summer migration of the intertropical convergence zone (ITCZ) and the associated IOM rainfall belt. Second, more than 90% of total annual precipitation (400 to 500 mm at the cave site) falls during the monsoon months (July to September), when dense clouds and mists cover the region. Presently, the cloud cover does not rise higher than 1500 m because of a temperature inversion created by the convergence between northwesterly winds and the low-level southwest monsoon winds (fig. S1A). As a result, monsoon precipitation occurs as fine drizzle, seldom exceeding more than 5 mm per day (unlike the heavy rains normally associated with strong convectional monsoonal rainfall) (8).

The time scale of the Q5 record is based on a total of 18 Th-U ages measured with thermal ionization mass spectrometry (TIMS) and multicollector inductively coupled plasma mass spectrometry (MC-ICPMS) (9) (tables S1 and S2; fig. S2). Stalagmite Q5 was deposited in two phases from 10.3 to 2.7 ky B.P. (the data are presented on the  $^{14}\text{C}$  absolute age scale where “present” is defined as 1950 A.D.) and from 1.4 to 0.4 ky B.P. (Fig. 1). The high-resolution  $\delta^{18}\text{O}$

profile is based on 1405 isotope measurements, sampled every ~0.7 mm along the center of the growth axis (10) (Fig. 1). Other stalagmite-based  $\delta^{18}\text{O}$  profiles from the same and from a neighboring cave confirm the Q5 record and indicate that sample- and site-specific noise is almost negligible (fig. S3, A and B).

Study of modern cave drip waters and stalagmites from Qunf Cave demonstrates that Q5 was deposited in or very close to isotopic equilibrium (11). Furthermore, our previous work on speleothems in Oman shows that speleothem  $\delta^{18}\text{O}$  values accurately reflect  $\delta^{18}\text{O}$  values of regional precipitation, and that changes in calcite  $\delta^{18}\text{O}$  over time primarily reflect changes in the amount of monsoonal precipitation (6, 12). As mentioned before, in Southern Oman strong convective cloud development is presently prevented by a temperature inversion (13), whereas the height of this temperature inversion is dynamically linked to the mean latitudinal summer position of the ITCZ and to the southwest monsoon wind pattern over southern Arabia (fig. S2A). A more northerly position of the ITCZ lifts the height of the temperature inversion, leading to stronger convective cloud development and higher monsoon precipitation over southern Oman (fig. S2B). Owing to the amount effect,  $\delta^{18}\text{O}$  values become more negative as rainfall increases. Hence, the Q5  $\delta^{18}\text{O}$  record can be regarded as a record of the amount of IOM precipitation, where the mean latitudinal summer position of the ITCZ over the Arabian Peninsula plays an important role.

The high-resolution  $\delta^{18}\text{O}$  profile of stalagmite Q5 shows four distinct features (Fig. 1). First, a rapid increase in monsoon precipitation between 10.3 and 9.6 ky B.P. is indicated by a sharp decrease in  $\delta^{18}\text{O}$  from  $-0.8$  to  $\sim -2\%$ . Second, an interval of generally high monsoon precipitation is observed between 9.6 and 5.5 ky B.P. with  $\delta^{18}\text{O}$  values averaging  $-2\%$ . Third, a long-term gradual decrease in monsoon precipitation starting at around 8 ky B.P. is indicated by a slow shift in  $\delta^{18}\text{O}$  from  $\sim -2.2\%$  at 8 ky to  $\sim -0.9\%$  (slightly more negative than  $\delta^{18}\text{O}$  values of modern stalagmites) at 2.7 ky B.P. (Fig. 1). Fourth, stalagmite deposition stopped at ~2.7 ky B.P. and restarted from between 1.4 and ~0.4 ky B.P. The  $\delta^{18}\text{O}$  values of the second growth phase lie within the range of modern stalagmites (Fig. 1). Superimposed on the long-term trend are distinct decadal and multidecadal second-order fluctuations in  $\delta^{18}\text{O}$  (Fig. 1).

In southern Oman the abrupt onset and rapid increase in monsoon precipitation between 10.3

<sup>1</sup>Institute of Geological Sciences, University of Bern, CH-3012 Bern, Switzerland. <sup>2</sup>Department of Geosciences, Morrill Science Center, University of Massachusetts, Amherst, MA 01003, USA. <sup>3</sup>Institute of Meteorology, University of Leipzig, D-04103 Leipzig, Germany. <sup>4</sup>Heidelberg Academy of Sciences, D-69120 Heidelberg, Germany.

\*To whom correspondence should be addressed. E-mail: dominik.fleitmann@geo.unibe.ch

REPORTS

and 9.6 ky B.P. indicate a rapid northward migration of the ITCZ and are in agreement with Arabian Sea upwelling records (4, 5) and regional lake level (3), ice core (14), and speleothem records (6, 12). Although some records (4, 5) indicate an initial increase in IOM strength between 13 and 12.5 ky B.P., there is no speleothem evidence in Oman for a monsoon intensification before ~10.3 ky B.P. (6, 12). The comparison between the Q5 and GRIP  $\delta^{18}\text{O}$  records (15) clearly reveals that the abrupt increase in monsoon precipitation is in phase with increasing air temperature in the northern Atlantic region (Fig. 2). When age uncertainties of  $\pm 1$  to 2% of the absolute age in both the Q5 and GRIP records are taken into account, decadal-scale intervals of reduced monsoon precipitation (more positive  $\delta^{18}\text{O}$  values) correlate with cooling events in Greenland and vice versa, as best expressed at 9.1 and 8.2 ky B.P. (15, 16) (Fig. 2). Although precise estimation of leads and lags is hampered by age uncertainties, the marked similarity between both records indicates that early Holocene IOM intensity was controlled on centennial and even on decadal time scales by glacial boundary forcing (e.g., Himalayan snow cover and North Atlantic sea surface temperatures). Such a strong teleconnection between low-latitude IOM variability and high-latitude temperature fluctuations during the late Pleistocene and last deglaciation is well known and was previously detected in marine cores from the Arabian Sea (4, 5, 17–19), but not in such detail for an early Holocene monsoon record.

After ~8 ky B.P., the gradual long-term decrease in monsoon precipitation (as inferred by the shift toward modern  $\delta^{18}\text{O}$  values) indicates a continuous southward migration of the mean summer ITCZ and a gradual weakening of monsoon intensity in response to declining June to August summer insolation at 30°N (20, 21) (Fig. 3A). A decrease in summer insolation reduced the land/sea thermal contrast and, therefore, the northward pull on the ITCZ and the monsoonal rainfall belt into the Arabian Peninsula. Supporting evidence for a gradual middle to late Holocene weakening in IOM wind strength and intensity is indicated by a decrease in abundance of *Globigerina bulloides* in an upwelling record from the Arabian Sea (Fig. 3B) (19). Additional evidence for an insolation-controlled gradual southward migration of the ITCZ during the Holocene has also been found for tropical South America (22) (10°43 N; 65°10 W), where decreasing Ti content indicates a long-term decline in summer precipitation (Fig. 3C). Taken together, these lines of evidence suggest that postglacial to modern precipitation patterns in the northern tropics are controlled, probably on a global scale, by the gradual southward migration of the ITCZ and gradual weakening of the monsoons in response to orbitally induced decreasing summer insolation.

Although in southern Oman monsoon precipitation continuously decreases from ~8 ky

**Fig. 1.** Q5  $\delta^{18}\text{O}$  record from southern Oman. Black dots with horizontal error bars are TIMS and MC-ICPMS Th-U ages (see tables S1 and S2). Black dot with vertical error bars and gray shaded area show the  $\delta^{18}\text{O}$  range of modern stalagmites (101 stable-isotope measurements during the past 50 years). Heavy gray line shows the long-term trend as defined by RAMPFIT (34) for the early Holocene and a sinusoidal in the late part.

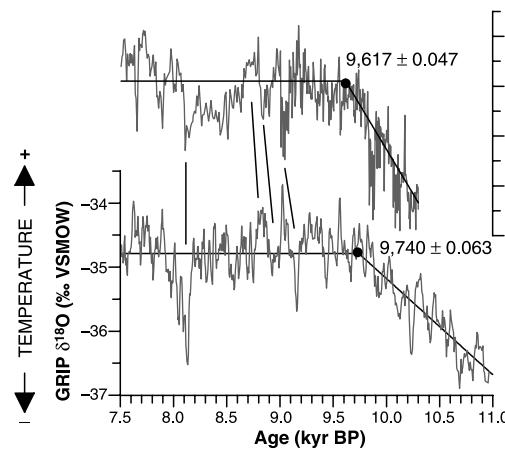
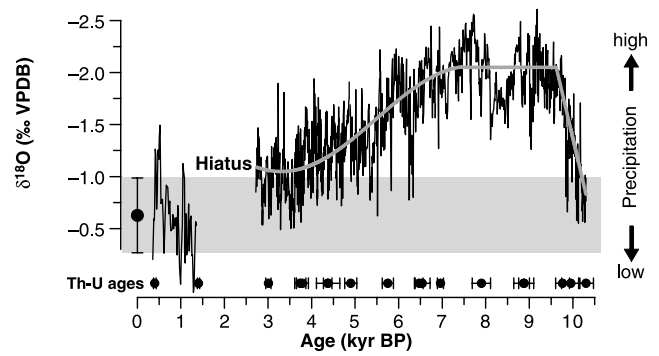


**Fig. 2.** Comparison of the Q5  $\delta^{18}\text{O}$  record with the smoothed (five-point running average) GRIP  $\delta^{18}\text{O}$  ice core record (15). Lower monsoon precipitation correlates with colder North Atlantic air temperatures (visualized by vertical tie-lines). The heavy black line shows "ramp" function trends (34). Change-point times are given with their statistical errors ( $1\sigma$ ), which are estimated from bootstrap simulations. Taking dating uncertainties for both the Q5 and GRIP records into account (1 to 2%) shows that the changes occurred simultaneously.

B.P. to the present, lake records in the African and Indian monsoon domain (1–3, 23) and a marine dust record off West Africa (24) rather suggest that monsoon precipitation decreased abruptly between 6 and 5 ky B.P. (Fig. 3D). How can we explain this apparent mismatch? First, both fully coupled (ocean-atmosphere-vegetation) climate model simulations (25) and geological data (3, 24) suggest that this abrupt humid-arid transition in northern Africa can be best explained by a threshold response (negative vegetation-atmosphere feedback) of the African monsoon to orbitally induced summer insolation. Second, lake levels in Indian monsoon domain may show a nonlinear response to precipitation changes. A shorter monsoon season and/or high-amplitude fluctuations in monsoon precipitation can quickly induce a negative precipitation-minus-evaporation balance, leading to rapid desiccation of the lake and, thus, terminating the record. Furthermore, lakes dry out as soon as the summer monsoonal rainfall belt retreats south of their drainage basin. We suggest that the Q5 record is, by virtue of its nature and geographical position, more suitable to record the gradual middle to late Holocene decrease in IOM intensity and precipitation. The Q5 record reveals an almost linear response of the IOM to orbitally induced variations in summer insolation after ~8 ky and, thus, confirms results of previously published climate model simulations (26).

Although during the early Holocene decadal to multidecadal changes in monsoon precipitation coincide with temperature fluctuations in the North Atlantic (Fig. 2), short-term fluctuations in IOM precipitation also occurred after 8 ky B.P. To examine the nature of these variations, we removed the long-term trend in the isotopic record by removing a sinusoidal fit to the later part (Fig. 1). We then compared the Q5 record to the tree-ring  $\Delta^{14}\text{C}$  record (27). The Q5 record was tuned—within the Th-U age uncertainties—to the  $\Delta^{14}\text{C}$  time scale [see (6) and fig. S4 for details]. The fine-tuned Q5  $\delta^{18}\text{O}$  isotopic record shows a strong similarity to the detrended  $\Delta^{14}\text{C}_{\text{res}}$  record (27), which largely reflects variations in solar activity (Fig. 4) (28, 29). In the fine-tuned Q5 record, intervals of weak (strong) solar activity correlate with periods of low (high) monsoon precipitation (Fig. 4). However, the visible correlation becomes less clear in the late Holocene when the  $\Delta^{14}\text{C}_{\text{res}}$  record shows only small amplitude variations in solar activity. Results of spectral analysis of both the detrended raw data and fine-tuned data further reinforce our interpretation that second-order variations in IOM precipitation were triggered by changes in solar activity, as indicated by statistically significant major solar cycles (within the 6-dB bandwidth) centered at ~220, ~140, ~107, 11, and 10 years for the untuned and ~240, ~140, ~90, ~18, and ~11 years for the fine-tuned  $\delta^{18}\text{O}$  paleoprecipitation

**Fig. 3.** (A) Smoothed (nine-point running average) Q5  $\delta^{18}\text{O}$  record and insolation curve (heavy black line) at  $30^\circ\text{N}$ , averaged from June to August (20, 21). (B) Indian monsoon upwelling record based on abundances of *G. bulloides* (19). Higher abundances of *G. bulloides* reflect more intense upwelling due to increased IOM wind strength. (C) Smoothed Cariaco Basin metal record (nine-point running average) (22). High Ti concentrations reflect higher river discharge due to increased summer precipitation. (D) ODP 658 terrigenous dust record from West Africa (24). High terrigenous dust concentrations reflect greater aridity in West Africa.

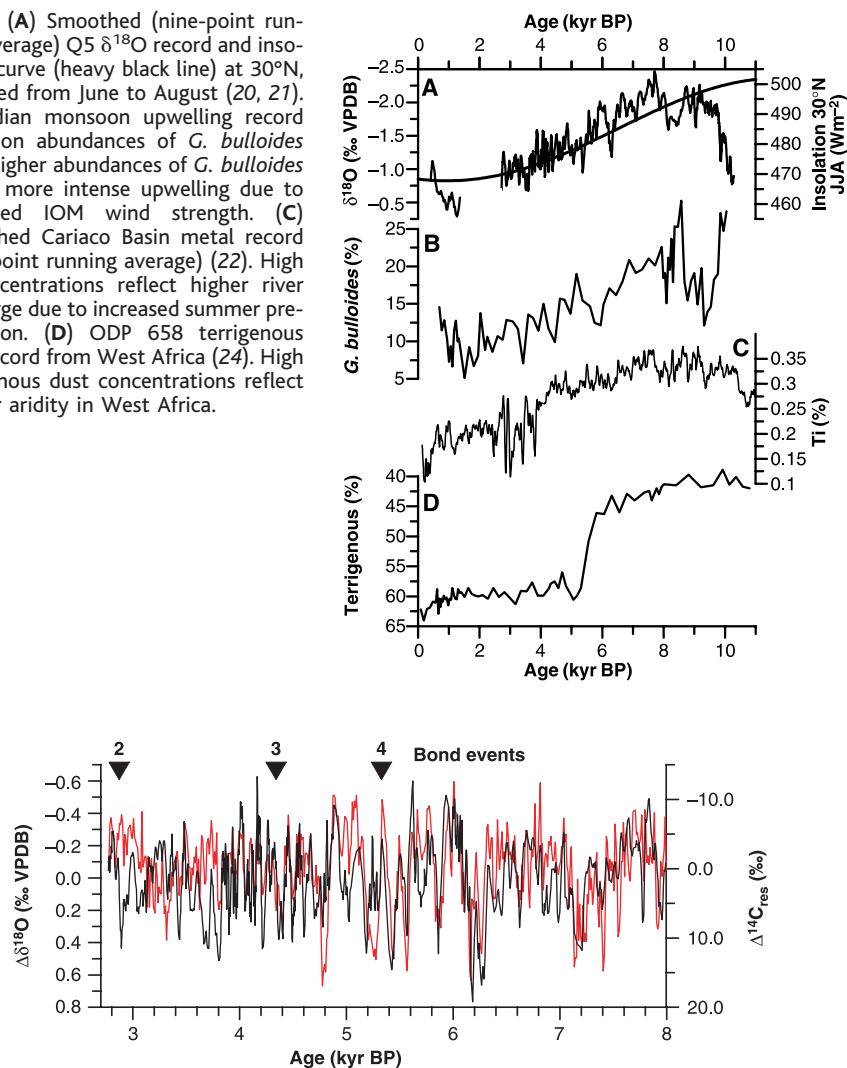


**Fig. 4.** Comparison between the detrended and smoothed (three-point running average) Q5  $\delta^{18}\text{O}$  (black line) and detrended atmospheric  $\Delta^{14}\text{C}_{\text{res}}$  (red line) profiles. The correlation coefficient between both records is  $r = 0.48$ . Labeled triangles are Bond events in the North Atlantic (31).

record (figs. S5, A and B). Additionally, the cross-spectral analysis between both records confirms the correspondence of statistically significant solar cycles at 205 (de Vries cycle), 132, 105, 90 (Gleissberg cycle), 60, and 55 years (fig. S5C). Such a close Sun-monsoon connection was previously detected in a shorter stalagmite record from northern Oman (6) and is now confirmed and extended by the much longer Q5 record from southern Oman. Whether variations in solar output affect the IOM indirectly, by internal forcing mechanisms (6, 19), or more directly, by external forcing mechanisms (30), is not yet fully resolved. Although solar-induced variations in the record of North Atlantic drift ice (termed Bond events) (31) may have influenced the IOM indirectly by way of the monsoon-Eurasian snow cover link during the early Holocene (6, 19), Bond events are less evident in the middle to late Holocene Q5 and marine upwelling record offshore Oman (19). This weak correlation may indicate that after 8 ky B.P.,

when the Northern Hemisphere ice sheets were largely gone and North Atlantic thermohaline circulation was more stable, IOM circulation responded more directly to changes in solar output (external forcing) than to changes in North Atlantic northward heat transport and deep-water production (internal forcing).

#### References and Notes

1. Y. Enzel *et al.*, *Science* **284**, 125 (1999).
2. H. A. McClure, *Nature* **263**, 755 (1976).
3. F. Gasse, *Quat. Sci. Rev.* **19**, 189 (2000).
4. F. Sirocko *et al.*, *Nature* **364**, 322 (1993).
5. J. Overpeck, D. Anderson, S. Trumbore, W. Prell, *Clim. Dyn.* **12**, 213 (1996).
6. U. Neff *et al.*, *Nature* **411**, 290 (2001).
7. S. J. Burns *et al.*, *J. Geophys. Res.* **107**, 4434 (2002).
8. I. D. Clark *et al.*, in *Use of Stable Isotopes in Water Resources Development* (International Atomic Energy Agency, Vienna, 1987), pp. 167–187.
9. Analytical procedures for the separation and purification of Th and U were performed as described in (32). Th-U measurements were in part performed on a MC-TIMS (Finnigan MAT 262 RPQ) and in part on a MC-ICPMS (Nu Instruments). TIMS measurements are described in detail in (6). The Nu Instruments

MC-ICPMS is equipped with three ion-counting electron multipliers, one of them placed behind a retardation (WARP) filter, and a Cetac Aridus desolvating nebulizer system. A mixed  $^{236}\text{U}$ - $^{229}\text{Th}$  spike was added before sample dissolution. U was measured in static mode, with ion counters for masses 236 and 234 and correcting for instrumental fractionation with the natural  $^{238}\text{U}/^{235}\text{U}$  ratio. Multiplier gains were calibrated with the National Institute of Standards and Technology U050 standard. Th was measured in a two-cycle sequence, measuring masses 230 and 229 alternately in the WARP-equipped multiplier, which was calibrated with an in-house Th standard. Doping with a Th-free solution of natural U enabled instrumental fractionation correction. The reproducibility of  $^{234}\text{U}/^{238}\text{U}$  ratios and  $^{232}\text{Th}$  concentrations is as given in (6) for the TIMS measurements. Activity ratios for MC-ICPMS data were calculated with the decay constants described in (33). This results in  $^{234}\text{U}$  activities 4‰ lower than previously used values. The resulting shift in ages is well within the experimental error.

10. For oxygen stable-isotope ratio determinations, ~5 mg of powder was drilled from the sample and analyzed with an on-line, automated carbonate preparation system linked to a VG Prism ratio mass spectrometer. Results are shown as the per mil difference between sample and the Vienna Pee Dee belemnite standard in delta notation. Reproducibility of standard materials is 0.08‰.
11. D. Fleitmann, S. J. Burns, A. Matter, *Eos* **80** (Fall meet. suppl.), abstract U11A-05 (1999).
12. S. J. Burns, D., Fleitmann, A. Matter, U. Neff, A. Mangini, *Geology* **29**, 623 (2001).
13. F. Sirocko, M. Sarnthein, H. Lange, H. Erlenkeuser, *Quat. Res.* **36**, 72 (1991).
14. L. G. Thompson *et al.*, *Science* **246**, 474 (1989).
15. W. Dansgaard *et al.*, *Nature* **364**, 218 (1993).
16. R. B. Alley *et al.*, *Geology* **25**, 483 (1997).
17. H. Schulz, U. von Rad, H. Erlenkeuser, *Nature* **393**, 54 (1998).
18. M. A. Altabet, M. J. Higginson, D. W. Murray, *Nature* **415**, 159 (2002).
19. A. K. Gupta, D. M. Anderson, J. T. Overpeck, *Nature* **421**, 354 (2003).
20. A. Berger, M.-F. Loutre, *Quat. Sci. Rev.* **10**, 297 (1991).
21. D. Paillard, L. Labeyrie, P. Yiou, *Eos* **77**, 379 (1996).
22. G. Haug, K. A. Hughen, D. M. Sigman, L. C. Peterson, U. Röhl, *Science* **293**, 1304 (2001).
23. F. Gasse, E. Van-Campo, *Earth Planet. Sci. Lett.* **126**, 435 (1994).
24. P. deMenocal *et al.*, *Quat. Sci. Rev.* **19**, 347 (2000).
25. M. Claussen *et al.*, *Geophys. Res. Lett.* **26**, 2037 (1999).
26. W. L. Prell, J. E. Kutzbach, *J. Geophys. Res.* **92**, 8411 (1987).
27. M. Stuiver *et al.*, *Radiocarbon* **40**, 1041 (1998).
28. J. Beer, W. Mende, R. Stellmacher, *Quat. Sci. Rev.* **19**, 403 (2000).
29. M. Stuiver, T. F. Braziunas, *Holocene* **3**, 289 (1993).
30. D. T. Shindell, G. A. Schmidt, M. E. Mann, D. Rind, A. Waple, *Science* **294**, 2149 (2001).
31. G. Bond *et al.*, *Science* **294**, 2130 (2001).
32. M. Ivanovich, R. S. Harmon, *Uranium Series Disequilibrium: Applications to Environmental Problems* (Clarendon, Oxford, 1993).
33. H. Cheng *et al.*, *Chem. Geol.* **169**, 17 (2000).
34. M. Mudelsee, *Comput. Geosci.* **26**, 293 (2000).
35. We thank D. Sanz for caving assistance and H. Al-Azry (Directorate of Minerals, Ministry of Commerce and Industry, Sultanate of Oman) for support during fieldwork. This work was supported by the Swiss National Science Foundation (grants 2021-52472.97 and 2000-059174.99) and the National Science Foundation of the United States (ATM-0135542).

#### Supporting Online Material

www.sciencemag.org/cgi/content/full/300/5626/1737/DC1  
 Tables S1 and S2  
 Figs. S1 to S5  
 References

5 February 2003; accepted 12 May 2003

## Supporting Online Material for Fleitmann *et al.*

### Supporting Tables

Table S1: Results of TIMS U/Th dating

Sample	depth [mm]	c(Th-230)		c(Th-232)		c(U-234)		c(U-238)		delta U-234		Age	
		[pg/g]	±	[ng/g]	±	[ng/g]	±	[µg/g]	±	[%o]	±	[kyr]	± [kyr]
Q5	2	0.033	0.002	1.660	0.012	0.023	0.0001	0.457	0.0022	-55.1	6.0	0.400	0.024
Q5	62.3	0.214	0.003	2.688	0.020	0.025	0.0001	0.488	0.0009	-63.9	3.4	3.010	0.057
Q5	140	0.300	0.009	0.777	0.007	0.029	0.0001	0.587	0.0012	-81.1	3.8	3.740	0.129
Q5	197	0.258	0.007	0.768	0.010	0.025	0.0001	0.490	0.0010	-67.3	6.0	3.790	0.138
Q5	259	0.339	0.013	2.998	0.069	0.027	0.0005	0.544	0.0035	-65.1	19.2	4.380	0.265
Q5	340	0.342	0.006	0.376	0.003	0.029	0.0001	0.579	0.0011	-82.3	4.4	4.370	0.105
Q5	428	0.390	0.008	2.374	0.021	0.029	0.0001	0.570	0.0011	-70.2	4.7	4.900	0.136
Q5	503	0.475	0.008	0.580	0.005	0.030	0.0002	0.617	0.0014	-85.8	5.0	5.750	0.134
Q5	574	0.538	0.012	1.223	0.011	0.030	0.0001	0.608	0.0013	-77.1	4.8	6.540	0.183
Q5	702	0.732	0.016	1.638	0.038	0.034	0.0001	0.696	0.0017	-86.7	3.5	7.910	0.213
Q5	780	1.135	0.023	38.85	0.416	0.041	0.0001	0.817	0.0024	-58.0	3.9	8.870	0.232
Q5	860	2.046	0.022	0.390	0.003	0.079	0.0003	1.585	0.0033	-76.7	3.7	9.760	0.155
Q5	903	2.062	0.030	0.940	0.009	0.077	0.0003	1.571	0.0037	-88.8	4.6	10.060	0.210
Q5	961	2.481	0.030	0.270	0.002	0.089	0.0002	1.827	0.0035	-90.9	2.8	10.470	0.170
S4	3	0.867	0.008	3.227	0.007	0.030	0.0001	0.605	0.0020	87.4	3.4	9.020	0.103
S4	87	0.542	0.007	1.787	0.013	0.022	0.0001	0.387	0.0010	49.4	4.7	9.150	0.168
S4	112	0.567	0.008	1.626	0.013	0.022	0.0001	0.388	0.0009	57.6	5.4	9.520	0.193
S4	209	0.637	0.006	2.683	0.005	0.028	0.0001	0.418	0.0010	53.5	3.8	9.930	0.202
S4	400	0.951	0.019	4.536	0.045	0.033	0.0002	0.595	0.0014	35.4	6.8	10.600	0.299

Table S2: Results of MC-ICPMS U/Th dating

Sample	depth [mm]	c(Th)		c(U)		$(^{234}\text{U}/^{238}\text{U})$		$(^{230}\text{Th}/^{232}\text{Th})$		$(^{230}\text{Th}/^{234}\text{U})$		Age	
		[ppb]	±	[ppb]	±	±	±	±	±	±	±	[kyr]	± [kyr]
Q5	40	2.164	0.012	664.9	1.8	0.9348	0.0007	11.83	0.14	0.0136	0.0002	1.400	0.030
Q5	565	3.334	0.022	606.3	1.6	0.9149	0.0010	28.88	0.32	0.0575	0.0005	6.470	0.090
Q5	627	1.641	0.009	632.9	1.6	0.9275	0.0008	66.58	0.58	0.0616	0.0005	6.960	0.080
Q5	762	0.449	0.003	676.2	1.7	0.9132	0.0009	324.13	3.58	0.078	0.0008	8.880	0.120
Q11	14	0.944	0.005	288.3	0.7	1.0288	0.0013	32.69	0.48	0.03447	0.00048	3.738	0.080
Q11	102	1.499	0.021	216.3	0.6	1.0267	0.0010	6.32	18.81	0.04207	0.00058	4.501	0.080
Q11	176	0.315	0.002	231.1	0.6	1.0212	0.0015	14.47	99.79	0.04414	0.00045	4.929	0.080

## Supporting Figures

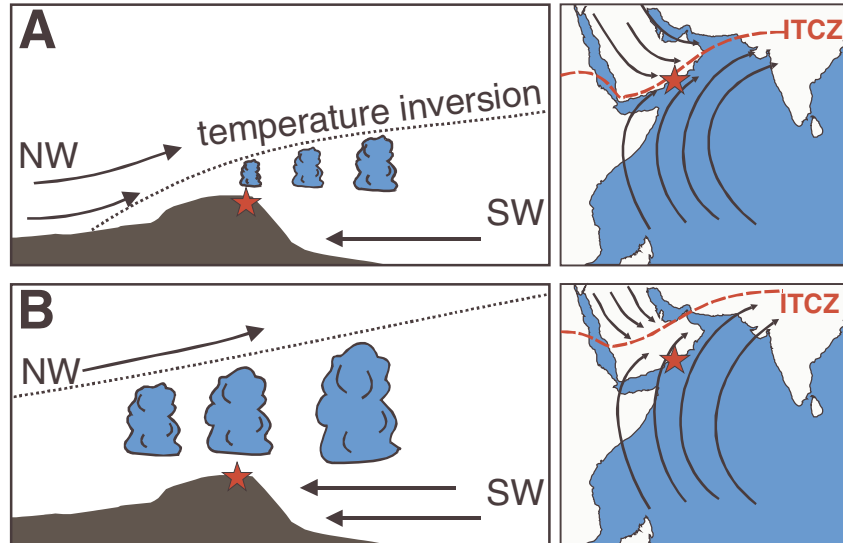


**Figure S1.** (A) Schematic figure of modern summer circulation pattern over Southern Oman. The red star shows the location of Qunf Cave. The black dashed line shows the position of the temperature inversion and the red dashed line the location of the ITCZ. (B) Schematic figure of summer circulation pattern at around 7 kyr BP.

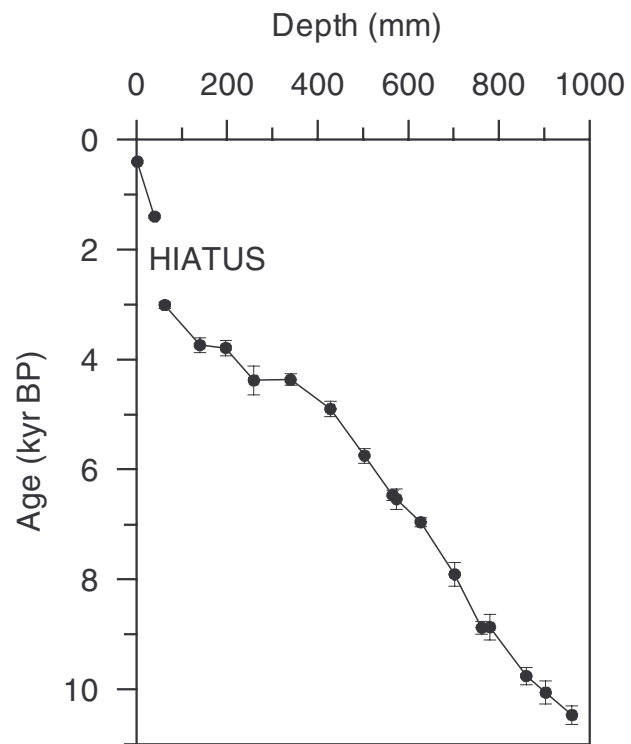


**Figure S2.** Plot of age versus depth for stalagmite Q5 (see Tables S1 and S2 for further details).

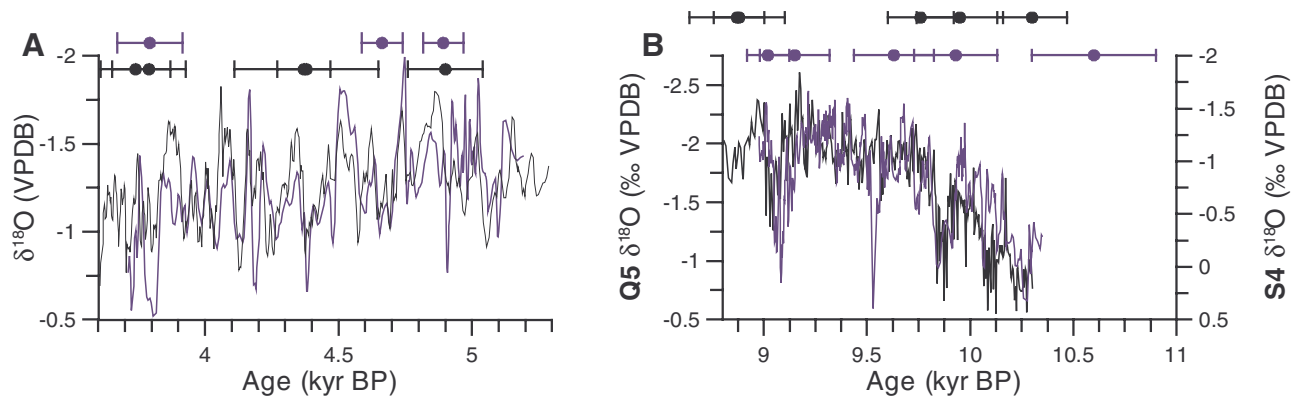


**Figure S3.** (A) Comparison of smoothed (3 point running average)  $\delta^{18}\text{O}$  profiles of stalagmites Q5 (black line) and Q11 (blue line) from Qunf Cave, and (B) of stalagmites Q5 (black line) and S4 (blue line). Stalagmite S4 was sampled in Kahf Defore (~150 m above sea level), approximately 40 km apart from Qunf Cave. Age calibration of stalagmite S4 is based on Th-U ages and annual growth band counts. The overall difference in  $\delta^{18}\text{O}$  between Q5 and S4 is caused by the altitude effect, which accounts for the observed difference of ~0.7‰. Error bars are color-coded Th-U ages.

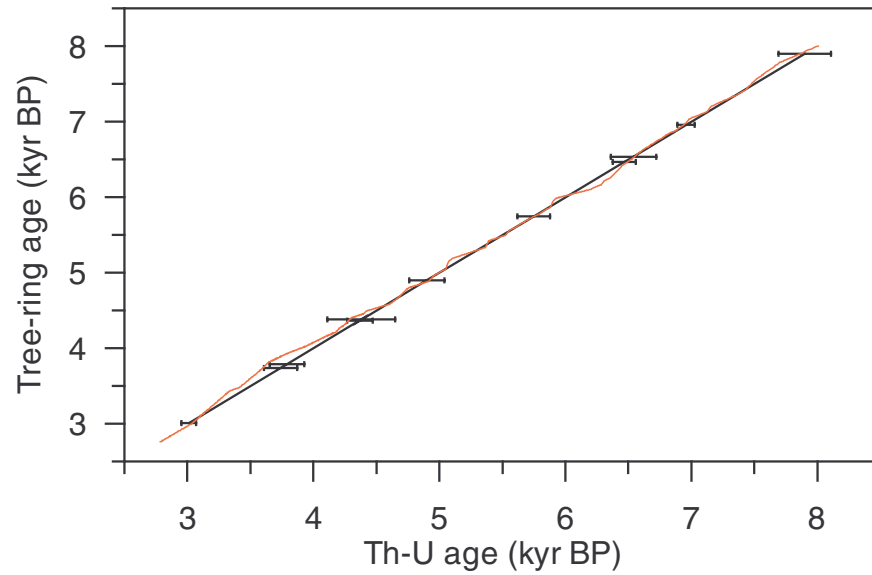


**Figure S4.** Measured (black line) and optimized (red line) Th-U age scales for stalagmite Q5. The error bars denote the uncertainties of the Th-U ages. The correlation between the time series of  $\delta^{18}\text{O}$  and  $\Delta^{14}\text{C}_{\text{res}}$  was made using the adjusted Th-U timescale. It is important to note, that the optimized timescale always remains within the uncertainty of the individual Th-U dates.

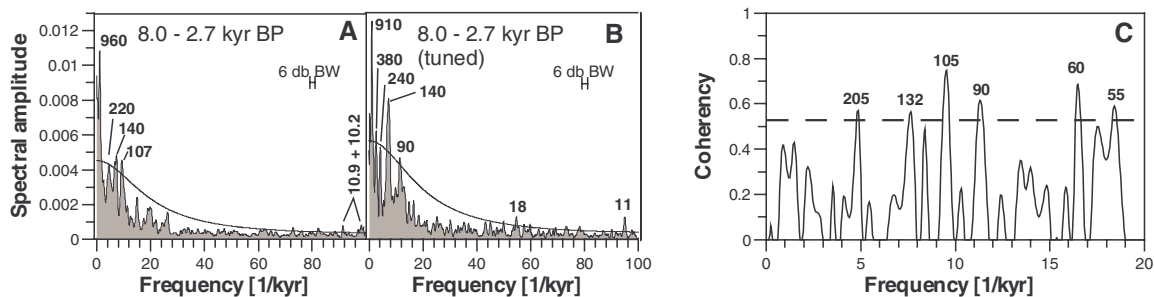


**Figure S5.** Univariate spectral analyses of the untuned (**A**) and tuned (**B**)  $\delta^{18}\text{O}$  time series from stalagmite Q5, and cross-spectral analysis (**C**) of tuned Q5  $\delta^{18}\text{O}$  time series and  $\Delta^{14}\text{C}$  measured in tree rings (*S1*) for the time interval up to 8 kyr BP. The Q5  $\delta^{18}\text{O}$  time series were detrended by removing a sinusoidal fitted to the late part (see Fig. 1), the polynomial detrended  $\Delta^{14}\text{C}$  time series (*S1*) prior to the analyses. The spectra were estimated using the Lomb-Scargle fourier transform for unevenly spaced data, the Welch-Overlapped-Segment-Averaging procedure (5 segments with 50% overlap), linear detrending for each segment, and a Welch I data taper. The univariate spectra (shaded in A and B) were bias-corrected using 2000 Monte-Carlo simulations (*S2*). Shown as red-noise alternative is upper 90% chi-squared bound (smooth line) of a first-order autoregressive (AR1) process. The AR1 process was fitted using the time-domain algorithm of ref *S3* to the  $\delta^{18}\text{O}$  time series subsequent to removal of harmonic peaks ( $> 1000$  yr period), yielding an equivalent autocorrelation coefficient of 0.57. This resulted in significant cycles at 960, 220, 140, 107, 10.9, and 10.2 yr period (**A**) and 910, 380, 240, 90, 18, and 11 yr period (**B**). The 6-dB bandwidth (BW), determining the frequency resolution, is  $1.06 \text{ kyr}^{-1}$  (**A**) and  $0.91 \text{ kyr}^{-1}$  (**B**, **C**). The coherency spectrum (solid line in **C**), calculated with an alignment of -400 yr of the  $\Delta^{14}\text{C}$  time series (*S4*), is compared against the 90% false-alarm-rate level (dashed line), resulting in significant coherent cycles at 205, 132, 105, 90, 60, and 55 yr period (**C**), as well as 32 and 24 yr period (not shown). The univariate spectra were calculated with software REDFIT (*S2*), the bivariate spectrum with SPECTRUM (*S4*); see those papers and references therein for further methodical details.

## References for Material and Methods

- S1. M. Stuiver *et al.* *Radiocarbon* **40**, 1041 (1998).
- S2. M. Schulz, M. Mudelsee, *Comput. Geosci.* 28:421 (2002).
- S3. M. Mudelsee, *Comput. Geosci.* **28**, 69 (2002).
- S4. M. Schulz, K. Stattegger, *Comput. Geosci.* **23**:929 (1997).